pH-Dependent Assembly of Tungsten Oxide Three-Dimensional Architectures and Their Application in Photocatalysis

Dandan Xu,[†] Tengfei Jiang,[†] Dejun Wang,[†,§] Liping Chen,[†] Lijing Zhang,[†] Zewen Fu,[†] Lingling Wang,*[,‡] and Tengfeng Xie*[,†]

[†]Physical Chemistry and [‡]State Key Laboratory of Supramolecular Structure and Materials, College of Chemistry, Jilin University, Changchun 130012, People's Republic of China

[§]Department of Chemistry, Tsinghua University, Beijing 100084, People's Republic of China

S Supporting Information

ABSTRACT: In this work, tungsten oxide (WO_3) with three-dimensional flower-like and wheel-like architectures, based on the spontaneous aggregation of one-dimensional nanorods, were successfully fabricated by adjusting the pH of the precursor solution. The influence of pH on the morphologies of WO_3 was systematically studied, and the different WO_3 architectures were used to photocatalytically degrade rhodamine B. The kinetic features of photoinduced charges of as-prepared WO_3 have been investigated by surface photovoltage spectroscopy and transient photovoltage techniques in detail. WO_3 with wheel-like and flower-like structures possess the higher charge separation efficiency and the lower recombination rate of photoinduced charges, resulting in higher photocatalytic activity for the degradation of RhB.

KEYWORDS: tungsten oxide, photocatalytic, transient photovoltage, surface photovoltage spectroscopy
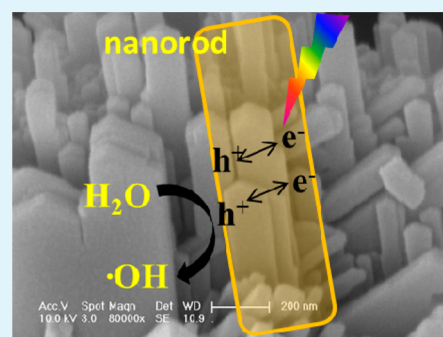
1. INTRODUCTION

Tungsten oxide (WO_3), an n-type semiconductor with an indirect band gap (2.6−3.2 eV), has attracted extensive research attention for its applications in electrochromism,[1−3] photochromism,[4] photocatalysis,[5,6] photoluminescence,[7] and gas sensing.[8,9] Above all, tungsten oxide represents an important photocatalyst and exhibits high photocatalytic activity for the degradation of organic compounds.[10,11] To meet the demand for diverse applications, much effort has been devoted to the controllable synthesis of tungsten oxide with particular morphologies, including one-dimensional (1D) nanorods[12] and nanowires,[13] three-dimensional (3D) hollow spheres, and hierarchically complex architectures.[14−16] It is well-known that one-dimensional structures can offer a direct path for the photogenerated charges, resulting in superior charge transport properties.[17,18] Recently, three-dimensional complex hierarchical structures forming via low-dimensional nanosized building block assembly have attracted more attention. And the 3D structures with a large void space are more beneficial for photocatalysis due to their large surface area and facile mass transport in materials.[19] Therefore, it is essential to develop facile approaches to synthesize 3D hierarchical structures in a controlled fashion.

However, fabrication of the micro/nanoarchitectures at the microscopic level is still a significant challenge. In recent years, scientists have made some advancement in fabricating 3D tungsten oxide nanostructures using different kinds of methods, such as chemical vapor deposition,[20] surfactant-assisted solvothermal,[14,21] and microwave assisted.[22] Although several types of tungsten oxide 3D structures with enhanced performance have been obtained, these methods used in synthesis processes usually require a special template.

In a previous report,[23] Wang and co-workers reported the synthesis of uniform crystalline WO_3 nanorods by a simple hydrothermal process in the absence of template and just adjusted the precursor solution to pH 2. In our work, the influence of pH on the morphologies of the products was systematically studied. We report the fabrication of tungsten oxide three-dimensional architectures consisting of one-dimensional nanorods. The as-prepared samples show highly efficient photocatalytic activity for the degradation of rhodamine B (RhB) under ultraviolet light illumination. Surface photovoltage spectroscopy (SPS) and transient photovoltage (TPV) techniques were used to study the behaviors of the photogenerated charges (including separation, transportation, and recombination) in the system.

2. EXPERIMENTAL SECTION

2.1. Synthesis of WO_3 Three-Dimensional Architectures. Sodium tungstate dihydrate ($Na_2WO_4 \cdot 2H_2O$), hydrochloric acid (HCl), and sodium chloride (NaCl) were used as the raw materials. All reagents are analytical grade and used without further purification. WO_3 three-dimensional architectures were synthesized by a hydrothermal process. A 0.825 g portion of $Na_2WO_4 \cdot 2H_2O$ and 0.290 g of

NaCl were dissolved in 75 mL of deionized water. Subsequently, 3 M HCl was slowly dropped into the solution with stirring until the pH value of the solution reached 1.5 and 2.0, respectively. Afterward, the solution was transferred into a Teflon-lined 100 mL capacity autoclave. Hydrothermal reaction was carried out at 180 °C for 24 h in an oven. After the autoclave was cooled to room temperature, product was obtained. At last, the products were centrifuged and washed with ethanol and distilled water three times and dried at 60 °C under air atmosphere for 10 h. In order to study the influence of pH on the morphologies, the reaction at other pH values was carried out. There is no precipitate when the pH is higher than 3.0. So we prepared the samples at four pHs (1.5, 2.0, 2.5, 3.0), which were denoted as WO_3-1.5, WO_3-2.0, WO_3-2.5, and WO_3-3.0, respectively. The time-dependent evolution experiments at pH 2.0 were conducted to study the formation mechanism of the sandwich structure.

2.2. Structural Characterization. The as-obtained products were characterized by X-ray diffraction (XRD) patterns on a Rigaku D/Max-2550 diffractometer with Cu Kα radiation (λ = 0.154 18 nm) over the range of $10° \leq 2\theta \leq 70°$. X-ray photoelectron spectroscopy (XPS) measurements were performed on a Thermo VG Scientific ESCALAB 250 spectrometer using monochromated Al Kα excitation. UV−vis diffuse reflectance spectroscopy (DRS) was recorded on a UV-3600 (Shimadzu) spectrophotometer. The morphology was obtained by a field emission scanning electron microscope (XL30 ESEM-FEG, FEI Co.). The specific surface area was analyzed by the Brunauer−Emmett−Teller (BET) method from nitrogen adsorption and desorption isotherms at 77 K using a Micrometrics ASAP 2420.

2.3. Photocatalytic Experimental. The photocatalytic activities of the as-prepared samples were evaluated by the degradation of the RhB under a high-pressure UV mercury lamp with 500 W illumination. Photocatalyst powder (20 mg) was dispersed into 20 mL of RhB solution (10 mg/L). Before illumination, the suspension was vigorously stirred in the dark for 60 min to ensure the adsorption−desorption equilibrium between the photocatalyst powder and the organic dye RhB. After that, the solution was irradiated by UV-light under magnetic stirring. The degradation of RhB was evaluated by centrifuging the retrieved samples and recording the intensity of the absorption peak of RhB (554 nm) relative to the intensity after stirring in the dark for 60 min (C/C_0) using a spectrophotometer. The degradation efficiency is equal to $1 − (C/C_0)$.

2.4. SPV Measurement. The SPV measurement was carried out on the basis of the lock-in amplifier.[24] The measurement system consists of a source of monochromatic light, a lock-in amplifier (SR830, Stanford Research Systems, Inc.) with a light chopper (SR540, Stanford Research Systems, Inc.), and a sample chamber. The monochromatic light is provided by passing light from a 500 W xenon lamp (CHFXQ500 W, Global Xenon Lamp Power) though a grating monochromator (Omni-5007, No.09010, Zolix), which chopped with a frequency of 24 Hz. All the measurements were operated at room temperature and under ambient pressure.

2.5. TPV Measurement. The TPV measurement was carried out to investigate the kinetics of the photoinduced charge carriers in our system. In our previous paper,[25] the TPV measurement was carried out in a device that was illustrated in detail. The samples were excited with a laser radiation pulse (wavelength of 355 nm and pulse width of 5 ns) from a third-harmonic Nd:YAG laser (Polaris II, New Wave Research, Inc.). The TPV signal was recorded by a 500 MHz digital phosphor oscilloscope (TDS 5054, Tektronix). The TPV measurements were finished in air atmosphere and at room temperature.

3. RESULT AND DISCUSSION

3.1. Structure and Morphology. The X-ray diffraction (XRD) patterns of WO_3 synthesized by hydrothermal treatment at different pH values are shown in Figure 1. Notably, all of the strong, sharp diffraction peaks of WO_3-2.5 and WO_3-3.0 can be indexed as the hexagonal phase of WO_3 with cell constants a = 0.7298 nm and c = 0.3899 nm, which are consistent with the values in the literature (JCPDS 33-1387). No other peaks for impurities are observed. When the pH value
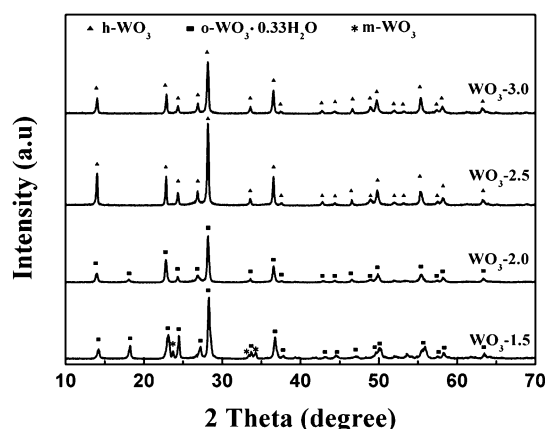

Figure 1. X-ray diffraction (XRD) patterns of WO_3 crystals synthesized by a hydrothermal route at different pH values (1.5, 2.0, 2.5, and 3.0).

decreases to 2.0, all peaks for WO_3-2.0 match orthorhombic WO_3·$0.33H_2O$ (o-WO_3·$0.33H_2O$, JCPDS 87-1203). Most peak locations of WO_3-1.5 are similar to those of WO_3-2.0 and also match those of o-WO_3·$0.33H_2O$. Meanwhile, three peaks located at 23.72°, 33.43°, and 34.28° are observed in WO_3-1.5 and are indexed as monoclinic WO_3 (m-WO_3, JCPDS 75-2072). As presented in Figure 1, at high pH, the product was h-WO_3. A further decrease of pH led to the formation of o-WO_3·$0.33H_2O$ and a mixture of m-WO_3 and o-WO_3·$0.33H_2O$ at pH 1.5.

The chemical states of element W for WO_3 prepared at different pH values are shown in the X-ray photoelectron spectroscopy (XPS). Figure S1 (Supporting Information) shows the W 4f core level spectrum of WO_3 prepared at different pH values. From the fitted peaks of W 4f, two main peaks were separated at 35.7 eV (W $4f_{7/2}$) and 37.8 eV (W $4f_{5/2}$),[26] which are indicative of W^{6+}. For all the samples, the valence states of W are +6 and no evidence of the W^{5+} state was found. Similar with our finding, Zhou et al. found no reduced tungsten state in hydrothermal o-WO_3·$0.33H_2O$.[27]

The optical property measurement of the as-prepared WO_3 samples (WO_3-1.5, WO_3-2.0, WO_3-2.5, and WO_3-3.0), using UV−vis diffuse reflectance spectroscopy (DRS), is shown in Figure 2. The absorption intensity has been normalized. It can be seen from Figure 2 that a red shift in the absorption appeared upon decreasing the pH value and the absorption
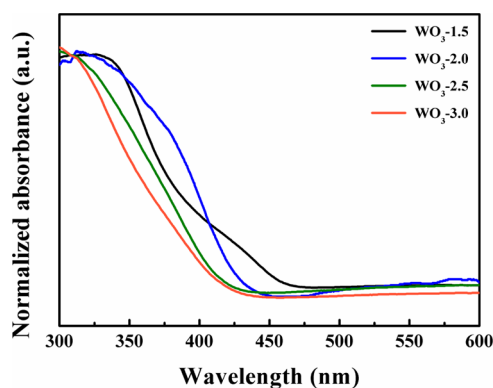

Figure 2. Normalized UV−vis absorption spectra of WO_3 synthesized at different pH values (pH 1.5, 2.0, 2.5, and 3.0).
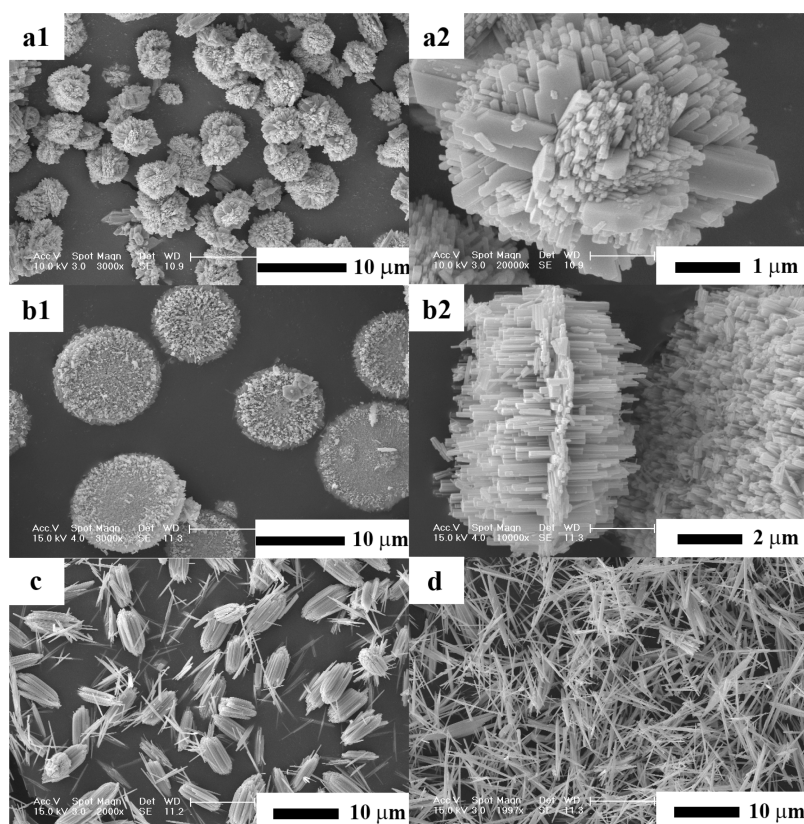
Figure 3. FESEM images of the as-prepared products synthesized at different pH values of the precursor solution: WO_3-1.5 (a1, a2), WO_3-2.0 (b1, b2), WO_3-2.5 (c), and WO_3-3.0 (d).
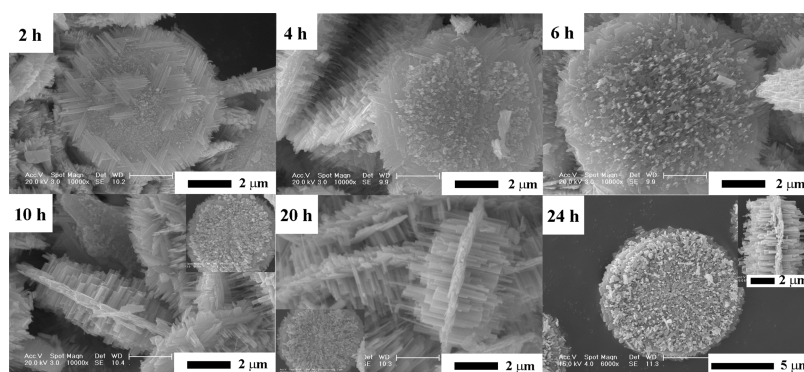

Figure 4. Time-dependent evolution of the WO_3 morphologies prepared at pH 2.0. FESEM images of the samples synthesized at different hydrothermal time intervals (2, 4, 6, 10, 20, and 24 h).

edge of WO_3-1.5 shifted to the visible-light region up to 460 nm.

The FESEM images of the as-prepared products synthesized by varying the pH value of the precursor solution are shown in Figure 3. It is clearly observed that the pH value plays an important role in controlling the morphology of the final products. Nanorod-based flower-like $WO_3\cdot0.33H_2O$ architectures 3−5 μm in diameter (Figure 3a1,a2) are obtained when pH value of the precursor solution is 1.5, and the surface of the nanorod is smooth, as shown in Figure S2a (Supporting Information). However, the morphology changes into wheel-shaped with many microscopic pores when the pH increases to 2.0, as seen in Figure 3b1. The image in Figure 3b2 shows the side of the wheel-like structure. We find it interesting that the wheel has a sandwich structure. In this sandwich, two outside

layers are bundles and the interlayer is a thin layer in which nanorods assemble horizontally. The bundle composes many nanorods with different length and the nanorod forms as particles stack (Figure S2b, Supporting Information). As displayed in Figure 3c, the specimen WO_3-2.5 comprises bundles and nanorods 5 μm in length, and there are some nanorods splitting away from the bundles. The WO_3-3.0 is made of numerous well-distinguishable WO_3 nanowires with a cylinder-shaped end, and the length of the wire is in the range of 7−10 μm (Figure 3d). All the surfaces of nanorods in WO_3-2.5 and nanowires are rough because of the stacked particles (Figure S2c,d, Supporting Information).

3.2. Morphological Evolution of the Wheel-like Structure of WO_3. According to the morphologies of samples prepared at different pH values, we find that in the sandwich
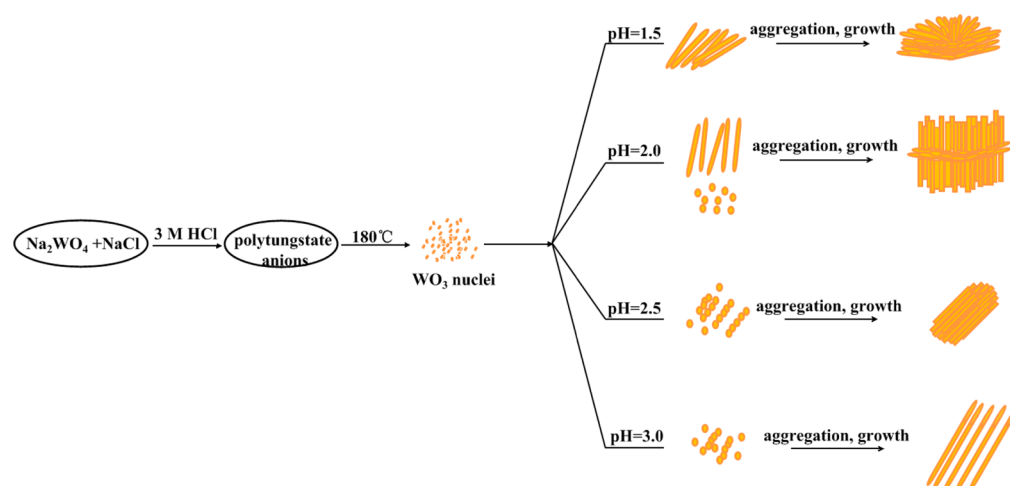
Figure 5. Schematic illustration of the growth process of WO$_3$.

structure of WO$_3$-2.0, the textures of the interlayer and two outside layers are different. The interlayer is similar to WO$_3$-1.5, with a smooth surface, while the two outside layers are similar to WO$_3$-2.5, which forms by particles stacking. WO$_3$-2.0 is the transition state. So we choose pH 2.0 to study the formation process in detail, and a series of contrast experiments in the case of WO$_3$-2.0 were also performed at different aging time at 180 °C. FESEM images of the samples synthesized at different hydrothermal time intervals are shown in Figure 4. After 2 h, a crystal with a disk shape is observed and it consists of many nanorods, and the surface of the nanorods of the interlayer is smooth. In addition, there are some small patches in the center of the disk, and pH of the residual solution in the autoclave changes from 2.0 to 2.14. When the reaction time is 4 h, some nanorods grow vertically on the disk, and the nanorods are short and uneven. Meanwhile, there is almost no change in the interlayer, and it keeps the same thickness. The pH value of the residual solution becomes 2.46, close to 2.5 (the initial pH of sample WO$_3$-2.5). With the reaction time increasing to 6 h, the density of nanorods becomes larger than at 4 h. From the image at 10 h, nanorods are longer with a length of 2 μm, and the number of nanorods increases. However, there is no real difference when the reaction time is further increased.

3.3. Growth Mechanisms of the WO$_3$ Prepared at Different pH Values. According to the FESEM results above, we can find that there are a few similarities in morphology between the adjacent two products. For WO$_3$-2.0, the shape and smooth surface of the nanorods in the interlayer are similar to those of WO$_3$-1.5. All the nanorods in the two outside layers of WO$_3$-2.0, WO$_3$-2.5, and WO$_3$-3.0 form by particles stacking. The reason for the regular evolution in morphology is that the pH value has an effect on the component of the precursor solution, further affecting the morphology. According to Chemseddine et al.'s report,[28] tungstate anions (WO$_4^{2-}$) protonize and polymerize, forming polytungstate anions in acid solution, and the structures of these anions are sensitive to the pH of the solution.[29] At pH 1−2, anions in the solution are in the form of tungstate Y (yellow) $[W_{10}O_{32}]^{4-}$. When the pH value is increased between 2 and 4, $[W_{10}O_{32}]^{4-}$ transforms into the Keggin structure metatungstate $[H_2W_{12}O_{40}]^{6-}$. Therefore, the precursor solution of WO$_3$-1.5 includes $[W_{10}O_{32}]^{4-}$, and that of WO$_3$-2.5 or WO$_3$-3.0 is $[H_2W_{12}O_{40}]^{6-}$ primarily. There are two components mentioned above at pH 2.0. According to morphological evolution of WO$_3$-2.0 with the sandwich

structure, the growing process of the crystals can be described. At the first stage, WO$_4^{2-}$ anions protonize and polymerize, forming polytungstate anions. At the second stage, the crystal nuclei of WO$_3$ microcrystals are produced at high temperature. There are two kinds of crystal nuclei, denoted as nuclei B, corresponding to $[H_2W_{12}O_{40}]^{6-}$, and nuclei A, corresponding to $[W_{10}O_{32}]^{4-}$. At the third stage, through continuous growth of the crystal nucleus, nuclei A grows into the nanorod with a smooth surface while nuclei B is stacked into the nanorod with a rough surface. The flower-like bundles and nanowire can be observed at the longer aging time. For WO$_3$-2.0, nuclei A evolved as disk-shaped crystal, while nuclei B grows into small microcrystals adhering to the disk's round side. More $[H_2W_{12}O_{40}]^{6-}$ anions form because the pH value increases[30] due to H$^+$ consumption during the reaction process. More nuclei B form and aggregate, developing into nanorods vertically on two round sides of the disk. As the reaction time increases, the number of nanorods increases and they become larger. Thus, WO$_3$ having a sandwich structure with a thin middle and thick outsides forms. So we propose a schematic illustration of the formation mechanism for WO$_3$ crystals at different pH values (Figure 5).

3.4. Photocatalytic Reaction. Photocatalytic activities of the as-prepared samples have been tested by the degradation of RhB under UV-light irradiation. To some extent, the large surface area is beneficial for photodegradation of organic dyes, which is proved in many report.[31,32] In this paper, we focus on the effect that the behaviors of photoinduced charges have on photocatalytic activity. The BET surface area of the as-prepared samples is listed in Table 1. In order to eliminate the factor of

Table 1. BET Surface Area of as-Prepared Samples

sample	WO$_3$-1.5	WO$_3$-2.0	WO$_3$-2.5	WO$_3$-3.0
BET surface area (m^2 g^{-1})	6.16	12.29	25.07	7.57

surface area, the photodegradation efficiencies of the same surface area for different samples were compared.[33] To be simple, we define that a unit of surface area is the same surface area. Photodegradation efficiency per unit surface area was calculated via dividing photodegradation efficiency by its surface area. As shown in Figure 6, the photodegradation efficiencies per unit surface area for WO$_3$-1.5 and WO$_3$-2.0 are

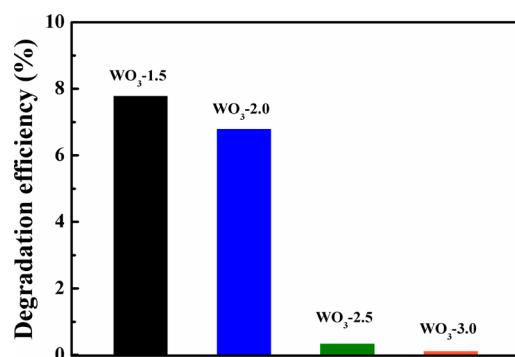nearly 1 order of magnitude higher than those of WO$_3$-2.5 and WO$_3$-3.0.

Figure 6. Photodegradation efficiencies per surface area for the four samples (WO$_3$-1.5, WO$_3$-2.0, WO$_3$-2.5, and WO$_3$-3.0) under UV-light irradiation for 1 h.

3.5. Photovoltaic Properties. The good understanding of photogenerated charge separation and transition properties in the WO$_3$ system may provide useful information for understanding the better performance in the photocatalytic process. Thus, SPS and TPV were employed to carefully investigate the photogenerated charge separation and transition properties of WO$_3$ photocatalysts. Figure 7 shows the SPV spectra of WO$_3$
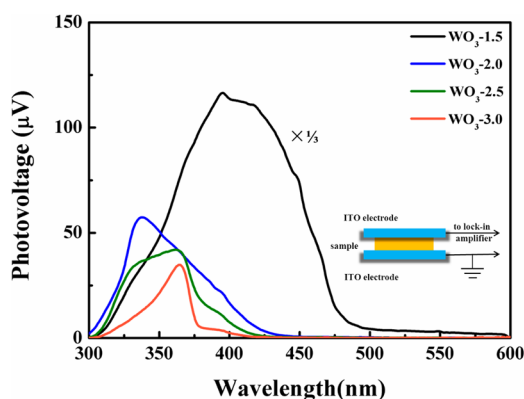

Figure 7. SPV spectra of WO$_3$ prepared at different pH values (1.5, 2.0, 2.5, 3.0). Inset: Schematic diagram of SPV measurement configuration. The real response intensity of WO$_3$-1.5 was reduced by 3 times in the spectrum.

prepared at different pH values. When WO$_3$ is irradiated under incident light with photon energy larger than its band gap, massive excess charge carriers are generated due to band-to-band transition. A SPV response starts to rise when photoinduced excess charge carriers are separated in space.[34] In Figure 7, we observe that all the samples have a positive SPV signal, which is a characteristic of n-type semiconductors. Meanwhile, there is a red shift in photovoltage response upon decreasing pH value, which is similar to UV−vis DRS (Figure 2). WO$_3$-1.5 has a distinct extension to visible light which is caused by monoclinic WO$_3$. In addition, WO$_3$-1.5 has a stronger signal than the other three samples. As we know, the value of SPV is proportional to the amount of charge (Q) separated spatially.[35,36] WO$_3$·0.33H$_2$O in particular is reported to have a strong affinity for water.[37] Upon illumination at a photon energy above the band gap, electron−hole pairs are

photogenerated. Holes migrate to the surface along the potential slope produced by band bending and are trapped by H$_2$O molecules that adsorb on the surface of WO$_3$·0.33H$_2$O in air atmosphere, producing hydroxyl radical ·OH. So the recombination rate of photogenerated electron−hole pairs is lower. It is demonstrated that there are more spatially separated charges for WO$_3$-1.5.

To further explore the photoinduced charge transfer behavior, the transient photovoltage (TPV) was measured. TPV measurement is a promising method for investigating the kinetics of photogenerated charge transfer.[38] It provides direct information about the generation, separation, and recombination of photogenerated charge carriers. Figure 8 shows the TPV
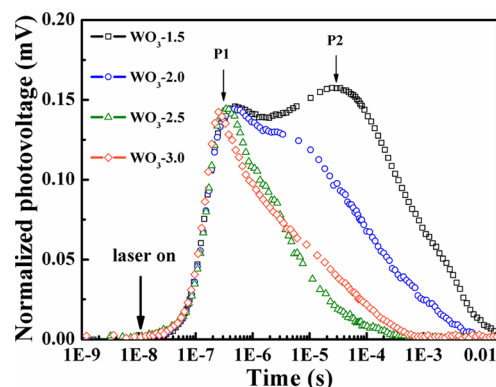

Figure 8. Photovoltage transients for the four samples (WO$_3$-1.5, WO$_3$-2.0, WO$_3$-2.5, and WO$_3$-3.0) for illumination with 355 nm (3.5 eV) laser pulses.

spectra of WO$_3$ prepared at different pH values, and all the intensities have been normalized. There is a remarkable feature that two peaks at a time shorter than 1×10^{-6} s (P1) and a time longer than 1×10^{-5} s (P2) can be observed in the TPV responses of WO$_3$-2.0 and WO$_3$-1.5. At P1, the TPV signal rises with the laser pulse for all samples, which is a typical feature of the surface photovoltage signal produced by the reduced surface band bending due to the neutralization of negatively charged surface states.[39] The TPV signal at P2 is typical for diffusion photovoltage.[40] In contrast, there is only one peak for WO$_3$-2.5 and WO$_3$-3.0 between 1×10^{-7} and 1×10^{-6} s. It is demonstrated that charges transportation is difficult in WO$_3$-2.5 and WO$_3$-3.0 because of the grain boundary barrier between nanoparticles. According to the TPV results, the following information can be obtained: the lifetime of photoinduced charge for WO$_3$ is prolonged with the decrease of pH, and the photocarrier lifetimes are 0.5, 0.3, 8, and 18 ms for WO$_3$-3.0, WO$_3$-2.5, WO$_3$-2.0, and WO$_3$-1.5, respectively. This means that WO$_3$-2.0 and WO$_3$-1.5 exhibit higher charge separation efficiency and lower recombination rate of charge carriers, which make the photoinduced charges possessing long lifetime participate in photocatalytic reactions.

According to SPV and TPV results, we attribute the higher photocatalytic activity for as-prepared WO$_3$ (WO$_3$-1.5 and WO$_3$-2.0) to higher charge separation efficiency and the longer photocarrier lifetime. However, the lifetime of photoinduced charges of WO$_3$-2.5 is smaller than that of WO$_3$-3.0 on TPV, while the SPV spectral response and photocatalytic performance of WO$_3$-2.5 are better than those of WO$_3$-3.0. The SPV response of WO$_3$-2.5 is higher than that of WO$_3$-3.0, which indicates the higher separation efficiency of photoinduced

charge for WO_3-2.5. We suppose that the lifetime does not dominate the overall photocatalytic performance, so it is the higher separation efficiency that results in higher photocatalytic performance.

4. CONCLUSIONS

In summary, we have successfully synthesized three-dimensional architectures via a hydrothermal route. The morphologies of the products can be tuned by adjusting the pH of the precursor solution. WO_3 with flower-like and wheel-like structure exhibit the higher photocatalytic activity in the degradation of RhB. It is demonstrated that effective separation and the longer photocarrier lifetime could be responsible for higher photocatalytic activity. We believe that these kinds of 3D flower-like and wheel-like sandwich structure WO_3 can be applied in many fields, for example, water purification, gas sensors, and solar energy cells.

■ ASSOCIATED CONTENT

Ⓢ Supporting Information

The X-ray photoelectron spectroscopy (XPS) (Figure S1) to study the chemical state of element W and the high-magnification FESEM images for WO_3 synthesized at different pH values (Figure S2). This material is available free of charge via the Internet at http://pubs.acs.org/.

■ AUTHOR INFORMATION

Corresponding Authors
*L.W. e-mail: ltlwll98003082@aliyan.com.
*T.X. e-mail: xietf@jlu.edu.cn.

Notes
The authors declare no competing financial interest.

■ ACKNOWLEDGMENTS

■ REFERENCES

(1) Zhang, J.; Tu, J. P.; Xia, X. H.; Wang, X. L.; Gu, C. D. Hydrothermally Synthesized WO_3 Nanowire Arrays with Highly Improved Electrochromic Performance. *J. Mater. Chem.* **2011**, *21*, 5492−5498.

(2) Park, S. Y.; Lee, J. M.; Noh, C.; Son, S. U. Colloidal Approach for Tungsten Oxide Nanorod-Based Electrochromic Systems with Highly Improved Response Times and Color Efficiencies. *J. Mater. Chem.* **2009**, *19*, 7959−7964.

(3) Balaji, S.; Djaoued, Y.; Albert, A.-S.; Bruening, R.; Beaudoin, N.; Robichaud, J. Porous Orthorhombic Tungsten Oxide Thin Films: Synthesis, Characterization, and Application in Electrochromic and Photochromic Devices. *J. Mater. Chem.* **2011**, *21*, 3940−3948.

(4) He, T.; Yao, J. Photochromic Materials Based on Tungsten Oxide. *J. Mater. Chem.* **2007**, *17*, 4547−4557.

(5) Sanchez Martinez, D.; Martinez-de la Cruz, A.; Lopez Cuellar, E. Photocatalytic Properties of WO_3 Nanoparticles Obtained by Precipitation in Presence of Urea as Complexing Agent. *Appl. Catal. A: Gen.* **2011**, *398*, 179−186.

(6) Yang, F.; Takahashi, Y.; Sakai, N.; Tatsuma, T. Photocatalytic Remote Oxidation Induced by Visible Light. *J. Phys. Chem. C* **2011**, *115*, 18270−18274.

(7) Su, X.; Li, Y.; Jian, J.; Wang, J. In Situ Etching WO_3 Nanoplates: Hydrothermal Synthesis, Photoluminescence and Gas Sensor Properties. *Mater. Res. Bull.* **2010**, *45*, 1960−1963.

(8) Vallejos, S.; Stoycheva, T.; Umek, P.; Navio, C.; Snyders, R.; Bittencourt, C.; Llobet, E.; Blackman, C.; Moniz, S.; Correig, X. Au Nanoparticle-Functionalised WO_3 Nanoneedles and Their Application in High Sensitivity Gas Sensor Devices. *Chem. Commun.* **2011**, *47*, 565−567.

(9) Lee, J. S.; Kwon, O. S.; Shin, D. H.; Jang, J. WO_3 Nanonodule-Decorated Hybrid Carbon Nanofibers for NO_2 Gas Sensor Application. *J. Mater. Chem. A* **2013**, *1*, 9099−9106.

(10) Bazarjani, M. S.; Hojamberdiev, M.; Morita, K.; Zhu, G.; Cherkashinin, G.; Fasel, C.; Herrmann, T.; Breitzke, H.; Gurlo, A.; Riedel, R. Visible Light Photocatalysis with c-$WO_{3−x}$/WO_3·xH$_2$O Nanoheterostructures in Situ Formed in Mesoporous Polycarbosilane−Siloxane Polymer. *J. Am. Chem. Soc.* **2013**, *135*, 4467−4475.

(11) Huang, L.; Xu, H.; Li, Y.; Li, H.; Cheng, X.; Xia, J.; Xu, Y.; Cai, G. Visible-Light-Induced WO_3/g-C_3N_4 Composites with Enhanced Photocatalytic Activity. *Dalton Trans.* **2013**, *42*, 8606−8616.

(12) Zhu, J.; Wang, S.; Xie, S.; Li, H. Hexagonal Single Crystal Growth of WO_3 Nanorods along a 110 Axis with Enhanced Adsorption Capacity. *Chem. Commun.* **2011**, *47*, 4403−4405.

(13) Phuruangrat, A.; Ham, D. J.; Hong, S. J.; Thongtem, S.; Lee, J. S. Synthesis of Hexagonal WO_3 Nanowires by Microwave-Assisted Hydrothermal Method and Their Electrocatalytic Activities for Hydrogen Evolution Reaction. *J. Mater. Chem.* **2010**, *20*, 1683−1690.

(14) Yan, A.; Xie, C.; Zeng, D.; Cai, S.; Li, H. Synthesis, Formation Mechanism and Illuminated Sensing Properties of 3D WO_3 Nanowall. *J. Alloys Compd.* **2010**, *495*, 88−92.

(15) Zhang, X.; Lu, X.; Shen, Y.; Han, J.; Yuan, L.; Gong, L.; Xu, Z.; Bai, X.; Wei, M.; Tong, Y.; Gao, Y.; Chen, J.; Zhou, J.; Wang, Z. L. Three-Dimensional WO_3 Nanostructures on Carbon Paper: Photoelectrochemical Property and Visible Light Driven Photocatalysis. *Chem. Commun.* **2011**, *47*, 5804−5806.

(16) You, L.; He, X.; Wang, D.; Sun, P.; Sun, Y. F.; Liang, X. S.; Du, Y.; Lu, G. Y. Ultrasensitive and Low Operating Temperature NO_2 Gas Sensor Using Nanosheets Assembled Hierarchical WO_3 Hollow Microspheres. *Sens. Actuators, B* **2012**, *173*, 426−432.

(17) Ma, D.; Shi, G.; Wang, H.; Zhang, Q.; Li, Y. Morphology-Tailored Synthesis of Vertically Aligned 1D WO_3 Nano-Structure Films for Highly Enhanced Electrochromic Performance. *J. Mater. Chem. A* **2013**, *1*, 684−691.

(18) Pilli, S. K.; Janarthanan, R.; Deutsch, T. G.; Furtak, T. E.; Brown, L. D.; Turner, J. A.; Herring, A. M. Efficient Photoelectrochemical Water Oxidation over Cobalt-Phosphate (Co−P$_i$) Catalyst Modified BiVO$_4$/1D-WO_3 Heterojunction Electrodes. *Phys. Chem. Chem. Phys.* **2013**, *15*, 14723−14728.

(19) Li, J.; Liu, X.; Han, Q.; Yao, X.; Wang, X. Formation of WO_3 Nanotube-Based Bundles Directed by NaHSO$_4$ and Its Application in Water Treatment. *J. Mater. Chem. A* **2013**, *1*, 1246−1253.

(20) Zhang, Y.; Chen, Y.; Liu, H.; Zhou, Y.; Li, R.; Cai, M.; Sun, X. Three-Dimensional Hierarchical Structure of Single Crystalline Tungsten Oxide Nanowires: Construction, Phase Transition, and Voltammetric Behavior. *J. Phys. Chem. C* **2009**, *113*, 1746−1750.

(21) Huang, J.; Xu, X.; Gu, C.; Fu, G.; Wang, W.; Liu, J. Flower-like and Hollow Sphere-like WO_3 Porous Nanostructures: Selective Synthesis and Their Photocatalysis Property. *Mater. Res. Bull.* **2012**, *47*, 3224−3232.

(22) Ma, Y.-L.; Zhang, L.; Cao, X.-F.; Chen, X.-T.; Xue, Z.-L. Microwave-Assisted Solvothermal Synthesis and Growth Mechanism of WO_3·0.33H$_2$O Hierarchical Microstructures. *CrystEngComm* **2010**, *12*, 1153−1158.

(23) Wang, J.; Khoo, E.; Lee, P. S.; Ma, J. Synthesis, Assembly, and Electrochromic Properties of Uniform Crystalline WO_3 Nanorods. *J. Phys. Chem. C* **2008**, *112*, 14306−14312.

(24) Zhao, Q.; Xie, T.; Peng, L.; Lin, Y.; Wang, P.; Peng, L.; Wang, D. Size- and Orientation-Dependent Photovoltaic Properties of ZnO Nanorods. *J. Phys. Chem. C* **2007**, *111*, 17136−17145.

(25) Wei, X.; Xie, T.; Peng, L.; Fu, W.; Chen, J.; Gao, Q.; Hong, G.; Wang, D. Effect of Heterojunction on the Behavior of Photogenerated Charges in $Fe_3O_4@Fe_2O_3$ Nanoparticle Photocatalysts. *J. Phys. Chem. C* **2011**, *115*, 8637−8642.

(26) Ranjbar, M.; zad, A. I.; Mahdavi, S. M. Real-time Measurement of Oxidation Dynamics of Sub-Stoichiometric Tungsten Oxide Films by Pulsed Laser Deposition. *Appl. Phys. A: Mater. Sci. Process.* **2008**, *92*, 627−634.

(27) Zhou, L.; Zhu, J.; Yu, M.; Huang, X.; Li, Z.; Wang, Y.; Yu, C. $Mo_xW_{1−x}O_3·0.33H_2O$ Solid Solutions with Tunable Band Gaps. *J. Phys. Chem. C* **2010**, *114*, 20947−20954.

(28) Chemseddine, A.; Bloeck, U. How Isopolyanions Self-assemble and Condense into a 2D Tungsten Oxide Crystal: HRTEM Imaging of Atomic Arrangement in an Intermediate New Hexagonal Phase. *J. Solid State Chem.* **2008**, *181*, 2731−2736.

(29) De Buysser, K.; Van Driessche, I.; Vermeir, P.; Thuy, T. T.; Schaubroeck, J.; Hoste, S. EXAFS Analysis of Blue Luminescence in Polyoxytungstate Citrate Gels. *Phys. Status Solidi B* **2008**, *245*, 2483−2489.

(30) Rozantsev, G. M.; Sazonova, O. I. Thermodynamic Parameters of Interconversions of Isopolyanions in Solutions of Tungsten(VI). *Russ. J. Coord. Chem.* **2005**, *31*, 552−558.

(31) Xiong, S.; Xi, B.; Qian, Y. CdS Hierarchical Nanostructures with Tunable Morphologies: Preparation and Photocatalytic Properties. *J. Phys. Chem. C* **2010**, *114*, 14029−14035.

(32) Dong, P.; Wang, Y.; Li, H.; Li, H.; Ma, X.; Han, L. Shape-Controllable Synthesis and Morphology-Dependent Photocatalytic Properties of Ag_3PO_4 Crystals. *J. Mater. Chem. A* **2013**, *1*, 4651−4656.

(33) Cho, S.; Jang, J.-W.; Kim, J.; Lee, J. S.; Choi, W.; Lee, K.-H. Three-Dimensional Type II ZnO/ZnSe Heterostructures and Their Visible Light Photocatalytic Activities. *Langmuir* **2011**, *27*, 10243−10250.

(34) Mora-Sero, I.; Dittrich, T.; Belaidi, A.; Garcia-Belmonte, G.; Bisquert, J. Observation of Diffusion and Tunneling Recombination of Dye-Photoinjected Electrons in Ultrathin TiO_2 Layers by Surface Photovoltage Transients. *J. Phys. Chem. B* **2005**, *109*, 14932−14938.

(35) Mora-Sero, I.; Dittrich, T.; Garcia-Belmonte, G.; Bisquert, J. Determination of Spatial Charge Separation of Diffusing Electrons by Transient Photovoltage Measurements. *J. Appl. Phys.* **2006**, *100*, 103705.

(36) Zabel, P.; Dittrich, T.; Funes, M.; Durantini, E. N.; Otero, L. Charge Separation at Pd−Porphyrin/TiO_2 Interfaces. *J. Phys. Chem. C* **2009**, *113*, 21090−21096.

(37) Daniel, M. F.; Desbat, B.; Lassegues, J. C.; Gerand, B.; Figlarz, M. Infrared and Raman Study of WO_3 Tungsten Trioxides and $WO_3·xH_2O$ Tungsten Trioxide Hydrates. *J. Solid State Chem.* **1987**, *67*, 235−247.

(38) Wei, X.; Xie, T.; Xu, D.; Zhao, Q.; Pang, S.; Wang, D. A Study of the Dynamic Properties of Photo-Induced Charge Carriers at Nanoporous TiO_2/Conductive Substrate Interfaces by the Transient Photovoltage Technique. *Nanotechnology* **2008**, *19*, 275707.

(39) Soudi, A.; Hsu, C.-H.; Gu, Y. Diameter-Dependent Surface Photovoltage and Surface State Density in Single Semiconductor Nanowires. *Nano Lett.* **2012**, *12*, 5111−5116.

(40) Timoshenko, V. Y.; Duzhko, V.; Dittrich, T. Diffusion Photovoltage in Porous Semiconductors and Dielectrics. *Phys. Status Solidi A* **2000**, *182*, 227−232.